

OBSERVATIONS OF DIFFERENTIAL CHARGING EFFECTS ON ATS 6

Richard Christopher Olsen
 Department of Physics, University of Alabama in Huntsville
 Huntsville, Alabama 35899

Carl E. McIlwain and Elden C. Whipple, Jr.
 Center for Astrophysics and Space Science, University of California at San Diego
 La Jolla, California 92093

Abstract. Differential charging effects observed in the electron data of the University of California, San Diego, auroral particles experiment on Applied Technology Satellite 6 are described and analyzed. An electrostatic barrier around the environmental measurements experiment (EME) package on ATS 6 is shown to be the natural result of dielectrics around the spacecraft which are more negatively charged than the main-frame of the spacecraft. In particular, the large dish antenna on ATS 6 causes the formation of a barrier which traps particles emitted from the EME package surface and returns them to the spacecraft. The insulating surface of the rotating University of Minnesota detector on the otherwise conducting EME package is shown to be the source of accelerated fluxes of electrons during charging events.

1. Introduction

Shortly after data started returning from ATS 6, it became clear that not only was the spacecraft charging negatively in sunlight, but large fluxes of electrons were being returned to the University of California, San Diego (UCSD) detector from the spacecraft surface. Work by Whipple [1976a, b] established that there was an electrostatic barrier returning secondary electrons and photoelectrons to the detectors, even when the spacecraft was charged to a negative potential. This barrier was shown not to be due to electron space charge effects, and it was postulated that the barrier was due to differential charging of spacecraft surfaces.

The science package on ATS 6 was almost entirely conducting, but large portions of the spacecraft surface were covered with insulators. In the work done to determine possible sources of the differential charging barrier, a number of possible surfaces were considered until the large dish antenna was shown to be capable of producing the observed barrier.

This identification is the focus of the first portion of the data presentation and analysis below. One other effect was studied in detail, the observation of intense fluxes of accelerated electrons near the energy of the differential charging barrier. One source of these particles was determined to be the University of Minnesota energetic particle detector, a small cube coated with an insulating white paint, located inside the barrier region, on the environmental measurements experiment (EME) box.

2. Spacecraft and Instruments

ATS 6 was launched into a geosynchronous orbit, initially stationed at 94°W near the geographic equator and about 10° north of the magnetic equator. It was a large spacecraft, with major dimensions of the order of 10 m, as illustrated in Figure 1. It can be seen that the dominant features are the large dish antenna, the solar-arrays extending out above the antenna, the earth viewing module (EVM) below the antenna, and the smaller environmental measurements experiment package above the antenna. The EVM and dish antenna were always oriented toward earth, so when the spacecraft was on the nightside of the earth, the top of the EME was in shadow.

The UCSD detectors are located on the EME package, as shown in the photograph in Figure 2. The detectors are differential in energy, angle, and time, covering the 1-eV to 80-keV energy range in 64 exponential steps in 16 s. The energy bandwidth is 20% of the selected energy, and the angular width is 2° by 5°. The two rotating heads sweep through a 220° range, with angles defined in Figure 3. The north-south head rotates in a plane through the spacecraft and the earth's axis, while the east-west head rotates in a plane perpendicular to the earth's axis [Mauk and McIlwain, 1975].

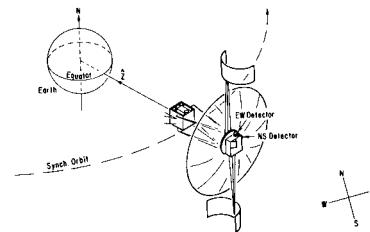


Fig. 1. Diagram of the ATS 6 spacecraft and its relationship to earth. The box on the earthward side of the spacecraft is the earth viewing module (EVM). The large parabolic dish antenna dominates the upper part of the satellite, with the solar arrays extending outward to the north and south of the craft. The environmental measurements experiment (EME) package sits on the portion of the satellite which perpetually points away from earth, and the UCSD detectors are located on the corner on the package.

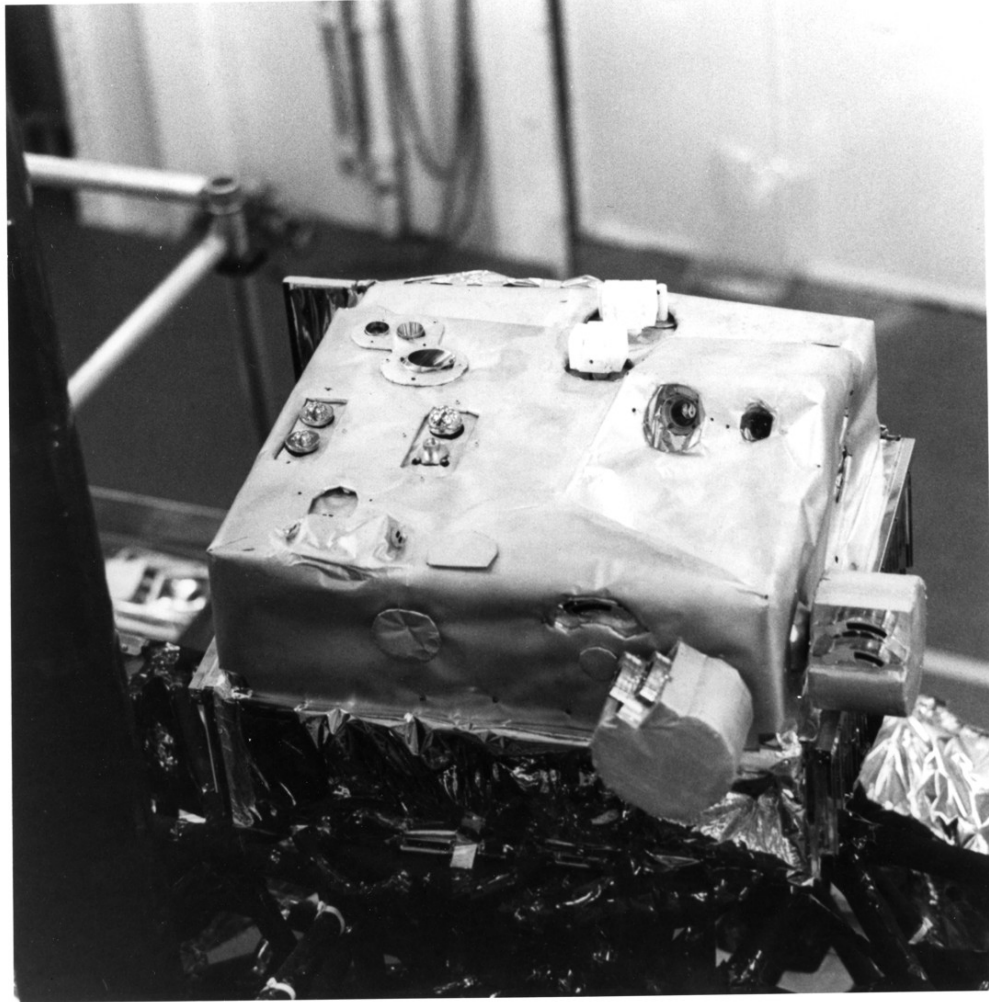


Fig. 2. Photograph of the EME package. The UCSD detectors sit on the lower right hand corner of the EME box. At the top center portion of the photograph, the two white boxes comprise the University of Minnesota detectors. The white box at the edge of the EME is the rotating UM detector.

The dish antenna is a complicated and important portion of the spacecraft structure. The antenna was composed of a dacron mesh, flashed with copper to create a conductor, then coated with silicon to aid deployment and maintain thermal control. This resulted in a large insulating surface below the science package. The antenna was folded at launch, and its successful deployment was one of the early achievements by a remarkable satellite.

The EVM carried the spacecraft systems, communications equipment, and the engineering experiments. Its surface was largely covered with a thermal blanket, with the insulating kapton surface facing outward. Substantial differential charging undoubtedly occurs on the EVM, and the spacecraft potential is probably largely determined by the EVM.

3. Barrier Observations

A good example of the observations of trapped electrons made on ATS 6 is shown in Figure 4, a spectrogram for 2 hours of data from the north-south detector. The detector shows electrons emitted from the surface returning to the spacecraft. The rotation of the north-south detector is reflected in the diagonal trace at the top of the spectrogram, which gives the pitch angle of the measured particles. The count rates are plotted with a gray scale, with black being zero count rate and white a maximum. The gray scale has an overflow provision for times when the count rate exceeds a maximum value, as is seen in the 40-eV ions between 0800 and 0805. The major features to be noted are the absolute spacecraft potential, which accelerates the ambient low-energy ions into the spacecraft at

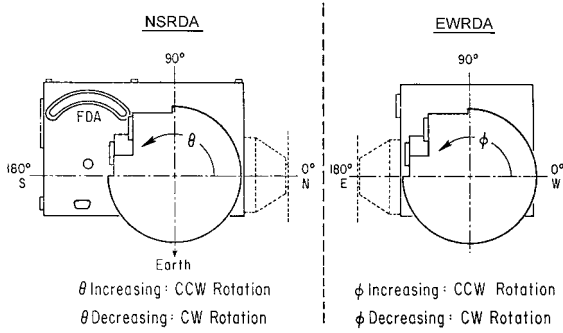


Fig. 3. Detector angle definition. The relative positions of the NS, EW, and FIX detectors are shown, along with the definition of the look directions. In both cases, 90° corresponds to looking radially outward from the spacecraft (and earth, see Figure 1.).

the spacecraft potential energy, and the high electron fluxes at energies which roughly mirror the spacecraft potential. The spacecraft potential is seen by the absence of ions below an energy ranging from 20 to 50 eV between 0720 and 0900. The differential charging signature is the bright white band of low-energy electrons over the same time period, reaching a maximum energy of 50-100 eV in the middle of the time period. The diagonal pattern along the barrier edge reflects the angular scanning pattern of the detector head. Other features in the spectrogram are the intense high-energy electron fluxes seen between 1 and 20 keV, which are the cause of the negative surface potentials, and vertical black stripes at slightly over 5-min intervals showing the obstruction of particles from the spacecraft.

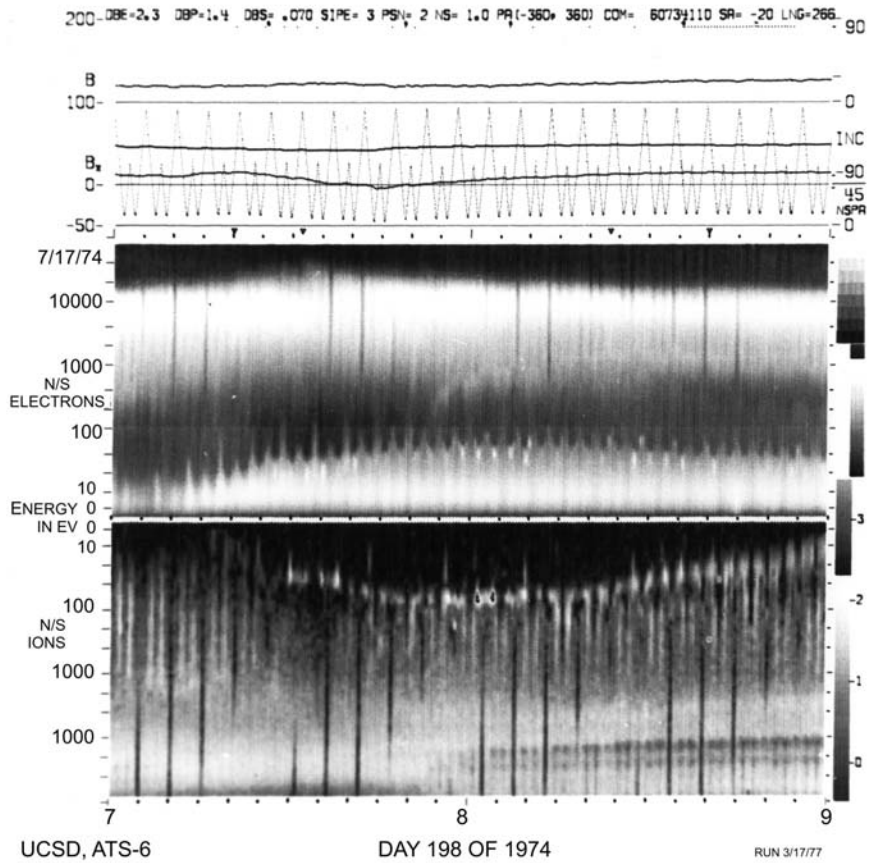


Fig. 4. Spectrogram for July 17, 1974. Two hours of data from the NS detector are shown. The gray scale corresponds to the intensity of the particle fluxes, with black a minimum and white a maximum. The energy scales are logarithmic above 10 eV, and both begin in the center of the figure, increasing to 80 keV. The diagonal line trace above the gray region is the pitch angle of the observed particles.

Bright vertical stripes at irregular intervals in the low-energy ions (below the space-craft potential energy) are believed to be ions generated near the spacecraft and returned to the spacecraft. These ions return at detector angles between 90° and 100° in both detectors and are apparently being accelerated from above the EME box into the spacecraft.

Looking in more detail at this data, we present the distribution functions from the three detector assemblies at 0756 UT. The distribution function, or phase space density, is proportional to the count rate divided by the square of the energy. Its most useful characteristic is that plasmas from different sources tend to give distribution functions with distinct breaks [Whipple, 1976b]. Most of the interesting features in the spectrogram are found here in Figures 5 and 6, for the electrons and ions, respectively. The breaks in the electron distribution functions in Figure 5 show that the division between spacecraft and ambient populations comes at 55 eV for the NS detector, and between 100 and 120 eV for the EW detector. A bump near 40 eV in the NS detector data is an example of the accelerated electron fluxes, called spots or spikes according to their appearance in spectrograms and line plots. They come from a spacecraft surface that is about -40 V away from the detector potential (described in section 5). Data from all three ion detectors are given in Figure 6. They show a typical ion charging spike in each detector at 55 eV. These fluxes are the thermal ions which have been accelerated into the space-craft. A flux of ions generated on or near the spacecraft appears in the NS detector between 10 and 40 eV, peaking at 25 eV.

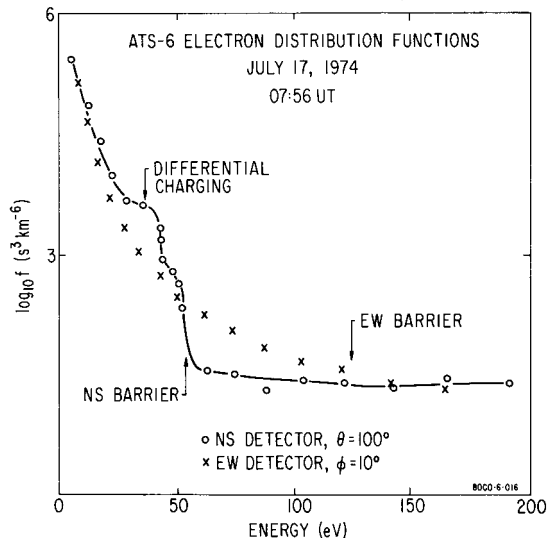


Fig. 5. Electron distribution functions for July 17, 1974, 0756 UT. The distribution functions (phase space density) for electron data from the two rotating detectors are shown here. The data from the NS detector were taken at a detector angle of 100°, and the data from the EW detector at 10°. The barrier height, as determined from these plots, is indicated for the two energy scans (4 s of data). The 'differential charging' bump in the NS data is a poor example of an accelerated flux of electrons below the electron barrier energy.

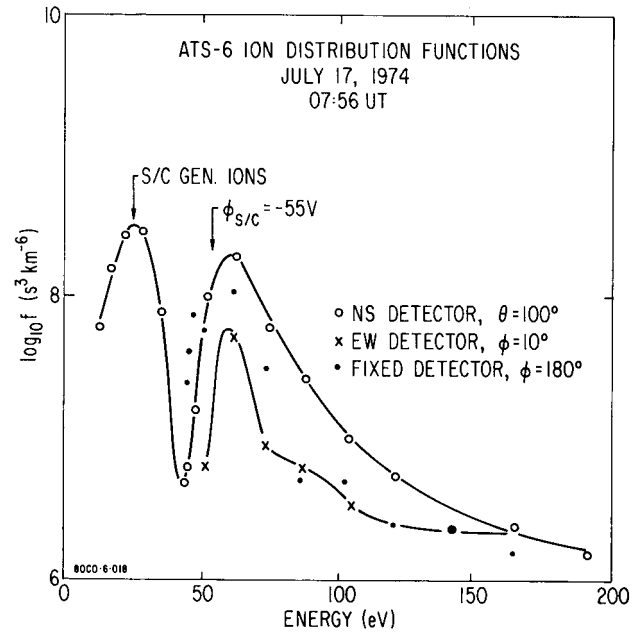


Fig. 6. Ion distribution functions for July 17, 1974, 0756 UT. The distribution functions for data taken from three ion detectors are shown. Fluxes vary above the spacecraft potential because of pitch angle variations. The peak seen in each trace at +50 to +60 eV is the signature of a spacecraft potential of about -55 V. The peak in the NS ion distribution function at 30 eV is due to a flux of ions generated on or near the spacecraft surface.

The angular dependences of the barrier heights in the two data sets are shown in Figure 7. The barrier height was taken to be the energy at which the electron distribution function had a distinct break or drop in value. This became difficult to determine at large detector angles. Detector angles are as defined in Figure 3, with 90° radially away from the spacecraft and 0° or 180° roughly tangential to the large dish antenna (see Figure 1). The north-south detector looks roughly along the solar array strut at very low angles. The two detectors both see a minimum in the barrier height when looking directly away from the spacecraft, and a poorly defined maximum when looking parallel to the antenna. The line traces over the data are two attempts to match the observed data with a monopole plus dipole model for the spacecraft potential distributions, as described below.

4. Barrier Modeling

Studies of charging, and particularly differential charging, by Prokopenko and Laframboise [1980] and others have shown that spacecraft in sunlight with large insulating surfaces will develop negative potentials on the shaded surfaces. Additional three-dimensional studies by Mandell et al. [1978] have shown that the resulting fields will then inhibit photoemission from sunlit surfaces and allow the entire spacecraft to charge negatively. A conducting

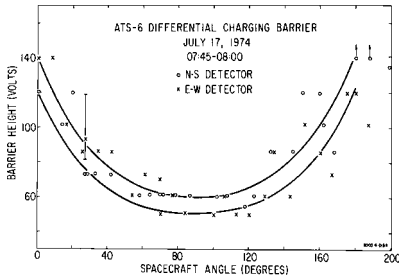


Fig. 7. Differential charging barrier height, July 17, 1974. The height of the electrostatic barrier around the EME package, as determined from the electron data, is plotted versus detector angle. Both rotating detectors are used. Line traces are the result of calculations using a spherical model to duplicate the angular variations in barrier height. The upper trace used parameters $V_m = -396$ V and $V_d = 341$ V; the lower used $V_m = -355$ V and $V_d = 300$ V.

spacecraft in sun-light, in geosynchronous environment, does not charge negatively, as demonstrated by GEOS (D. Young, private communication, 1980) and ISEE. The differential potentials responsible for the barrier are maintained during the charging of the spacecraft. With this background of theory in hand, we now attempt to model the observations. A simple spherical model is shown first, then the more complicated NASA charging analyzer program model is applied.

Monopole Plus Dipole Model

Differential charging effects can be illustrated with a model which combines a monopole and dipole potential distribution on a sphere. Such a model was recently demonstrated by Besse and Rubin [1980]. This model is used here to match the angular variations in barrier height found in the data. The model uses a spherical object with cylindrical symmetry, and a surface potential given by

$$\Phi(R,\Theta) = V_m + V_d \cos(\Theta)$$

where R is the sphere radius, V_m is the monopole voltage (the potential at the center of the sphere), V_d is the dipole voltage (the potential difference between the top and center), and Θ is the angle from the z axis. These terms are similar to but not identical to the first two terms in a multipole expansion of an arbitrary potential distribution. The monopole potential is the average over the sphere; the dipole potential is half the differential potential from top to bottom. The potential away from the sphere is

$$\Phi(r,\Theta) = V_m (R/r) + V_d \cos(\Theta) (R/r)^2$$

One difference between the use of the model here and that of Besse and Rubin is that particle trajectories are used to determine the height of the electrostatic barrier for particles emitted from or incident on the top of the sphere.

This model was applied to the above observations. The sum of the monopole and dipole voltages was set equal to the spacecraft potential, providing one constraint on the two variables.

MONOPOLE + DIPOLE MODEL
POTENTIAL CONTOURS

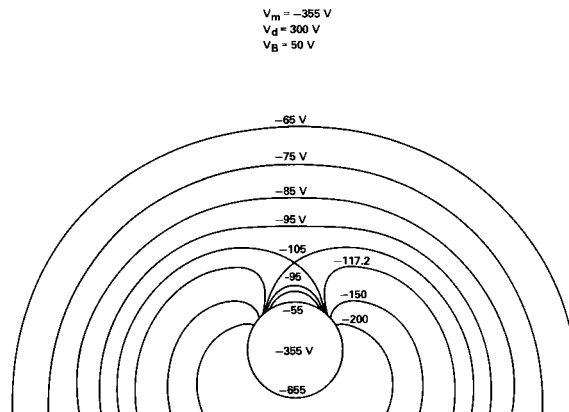


Fig. 8. Monopole plus dipole model potential contours. Potential contours for a spherical object with imposed potentials of $V_m = -355$ V and $V_d = 300$ V are shown. A saddle point is formed above the sphere at a potential of -105 V. The top of the sphere is at -55 V.

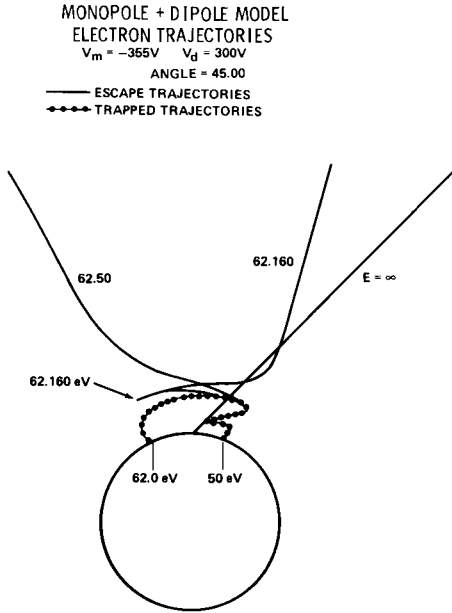


Fig. 9. Monopole plus or minus dipole model electron trajectories. The particle trajectories for electrons in the potential distribution of Figure 8 are shown here. Particles leave the top of the sphere at an angle of 45° (shown by the $E = 03$ trace). Dotted trajectories (50 and 62.0 eV) are trapped.

The two voltages were then varied to obtain the observed barrier height. The potential distribution and resulting particle trajectories are shown in Figures 8 and 9 for the case of the lower barrier height (the lower trace in Figure 7) using $V = -355$ V and $V_d = 300$ V. This resulted in a 50-V

barrier at 90°, doubling to 100 V by 170°. The potential distribution, shown in Figure 8, is fairly straightforward. The top of the sphere, at -55 V, represents the observation point, and the saddle point at -105 V the minimum in the barrier height. The barrier height for particles incident at other than 90° is then determined by particle tracking, with a sample shown for 45° in Figure 9. Particles with less than 62.16-eV energy are reflected back to the top of the sphere. The 62-eV particles turn at the -117-V equipotential, shown in the potential plot. Note the variations in angle for the two escaping trajectories. Particles with only slight differences in energy follow substantially different trajectories. The effect of the dipole field becomes greater at larger angles, as the angular momentum imparted by the dipole becomes more important. The higher barrier (the upper trace in Figure 7) was obtained using $V_m = -396$ V and $V_d = 341$. This produced a 60-V barrier at 90°, doubling again by 170°. The two pairs of parameters result in a -55-V potential at the top of the sphere and a -655 to -740-V potential at the bottom of the sphere. This implies a differential potential across the spacecraft of between 600 and 680 V, which is difficult to compare to the data but not unreasonable for a shadowed surface in this environment. This success in matching the observed barrier structure and magnitude with a simple model suggests that differential charging is indeed responsible.

NASCAP Model

The monopole plus dipole model discussed above has the advantage of being easy to use for calculating particle trajectories. It does not do a good job of simulating the spacecraft geometry, and a different code was used to complete the barrier source identification.

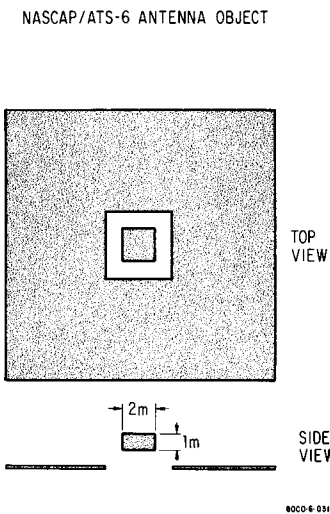


Fig. 10. NASCAP/ATS 6 antenna object. The object defined to study potential contours around the ATS 6 EME package is shown here. The inner box is to represent the EME, and the large plane the dish antenna.

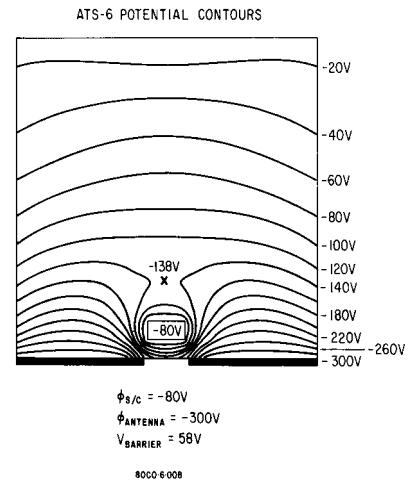


Fig. 11. NASCAP/ATS 6 object potential contours. Equipotential contours shown around the object defined in Figure 10 in order to duplicate the daylight charging observed on September 8, 1974. A potential of -300 V is applied to the antenna, and -80 V to the EME box. A saddle point forms above the EME at -138 V.

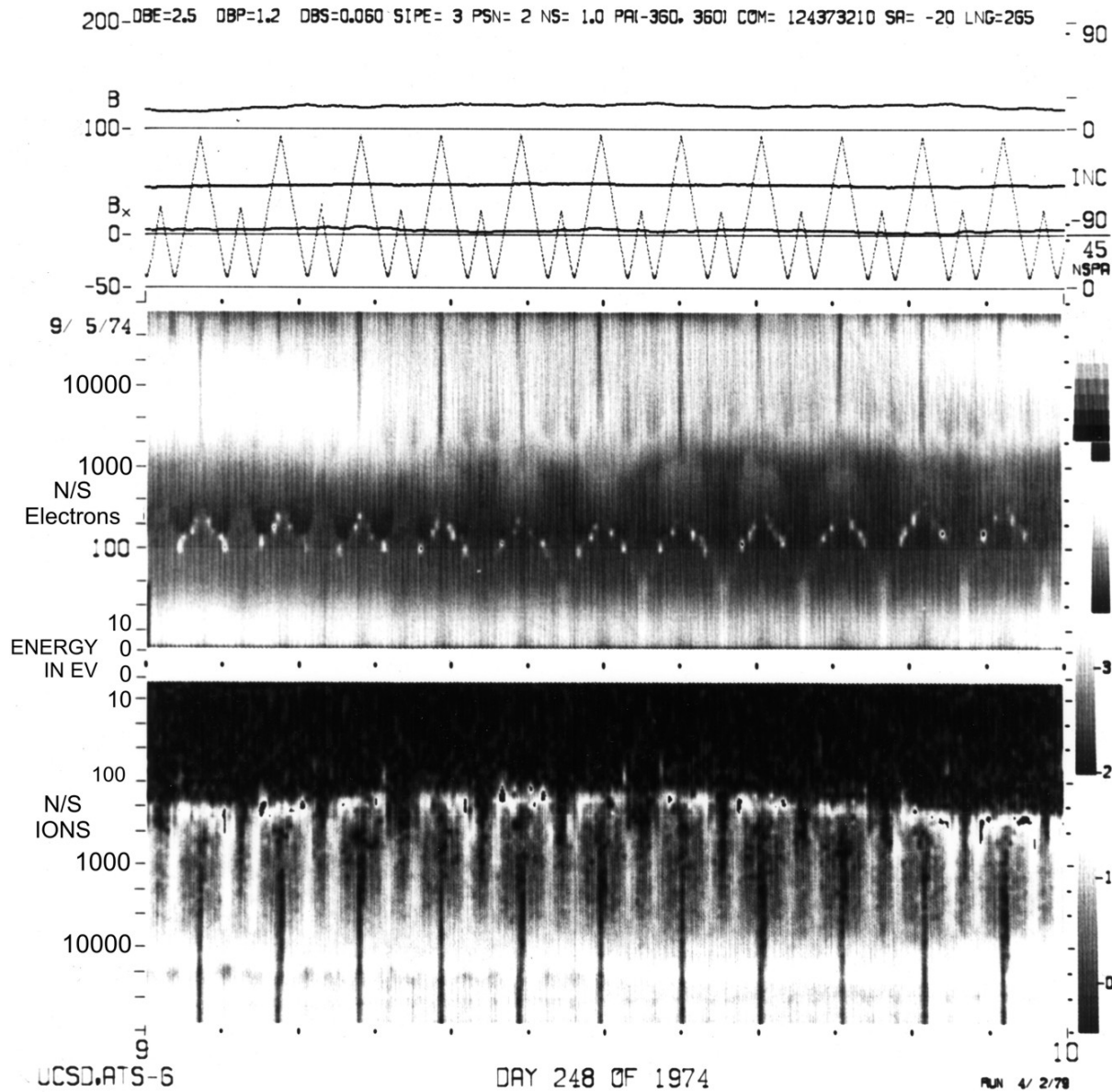


Fig. 12. Spectrogram for September 5, 1974. One hour of data from the NS detector is shown.

The NASA charging analyzer program (NASCAP) [Mandell et al., 1978] is a three-dimensional code which is capable of establishing an object in a 16 x 16 x 32 grid and solving for the potentials on and currents to spacecraft surfaces in magnetospheric environments. The potential solver portion of this code was used to model the spacecraft, and to attempt to generate a barrier to electrons by means of differential surface potentials.

Early runs with large negative potentials on the solar arrays showed that they were too far from the EME package to generate a barrier around it. The next attempt, an idealized model of the dish antenna and EME package, was very successful in generating fields which would give the observed behavior. The geometric model used in the field calculations is shown in Figure 10. The small box in the center is

the EME, while the large grid is the antenna. Each was fixed at a potential, and the code was allowed to solve for the resulting fields. The large equipotential surface was found to overwhelm the smaller EME surface area. Barriers to charged particles of height similar to the differential potential were found in most runs. A case of -50-V spacecraft potential and -100-V antenna potential was found to generate a 3-V barrier for example.

A further test of the identification of the antenna as the barrier source requires a more accurate knowledge of the mainframe and insulator potentials for an observed case. The antenna potential is not known, however, and the best we can do is to apply the model and ask if the potential

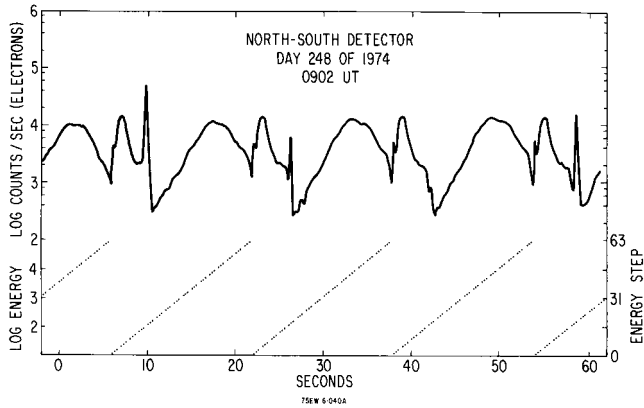


Fig. 13. Line plot for September 5, 1974, 0902 UT. One minute of data is shown from the NS electron detector. The upper, dark line is the count rate, plotted on a logarithmic scale. The dotted lines below indicate the 64-step energy scan from 0 to 80 keV.

necessary for a barrier is reasonable. We use a barrier observation made shortly after an eclipse as a case where the eclipse potential of the main-frame, if not the insulators, is known. Data from September 8, 1974, were chosen for the smoothness of the environment and a nearly constant eclipse potential of -4000 V. Shortly after exiting eclipse (2-3 min), the spacecraft had risen to -80 V, and a differential charging barrier of 60 V at 90° spacecraft angle was visible in the electron data.

This case was modeled with NASCAP with -80-V potential on the spacecraft and -300-V on the antenna. The -300-V potential was a compromise between the observed eclipse potential of the spacecraft and the observed sunlight potential of the spacecraft. Experience with this model and some luck eliminated the need to try other potentials. This model run, shown in Figure 11, resulted in a barrier height of 58 V. This is a remarkable agreement with the data.

The same barrier height could be produced with the monopole plus dipole model with values $V_m = -463$ V and $V_d = 383$ V. This implies a differential voltage of 383 V from top to middle, which is larger than the 220-V difference used in the NASCAP model. This shows some of the effect of the near-planar geometry of the NASCAP model as compared to the spherical model. In either case, the inferred insulator potential is substantially less negative than in eclipse, suggesting that processes which limit the differential potential are important. Likely candidates are leakage currents on and over insulator surfaces.

NASCAP runs were made with potential distributions on the antenna which were not equipotentials. As long as the potentials were more negative than the spacecraft, a barrier was created. The fields in these runs were distorted, and the saddle point was off center.

The result of these barrier calculations is the identification of the antenna as the source of the differential charging barrier seen around the UCSD detectors and the EME package. This barrier is not necessarily the same barrier that is controlling the spacecraft potential, since not all of the conducting surface areas of the spacecraft are on the EME package. Other conducting areas are the struts supporting the solar arrays and some portions

of the EVM. The charging dynamics of the insulators around these surfaces are the same, however, and they are believed to behave in the same way.

5. Accelerated Electron Fluxes

A phenomenon related to differential charging is the presence of accelerated electron fluxes at an energy near the barrier height. These fluxes are narrowly confined in energy and angle. They have been called spikes or spots according to their appearance in line plots and spectrograms, respectively.

A clear case is shown in Figure 12, a 1-hour spectrogram from September 5, 1974 (day 248). The environment is highly energetic, with large electron fluxes up to 80 keV, but relatively constant in time, as reflected in the constancy of the spacecraft potential at -200 V. The north-south detector is rotating, and the barrier height is varying between 100 and 200 V. The bright spots tracing the outline of the barrier are the accelerated fluxes of interest. The black stripes are due to the detector looking at one of the solar array struts at one end of its rotational pattern.

Data from this time period are presented in three more plots, in Figures 13, 14, and 15. Figure 13 is a plot of the count rate versus time for 1 min of data at 0902. The dotted lines show the scan in energy while the solid line is the electron count rate. A typical scan begins at 6 s, and runs to 22 s. At low energies, there is a bump due to trapped

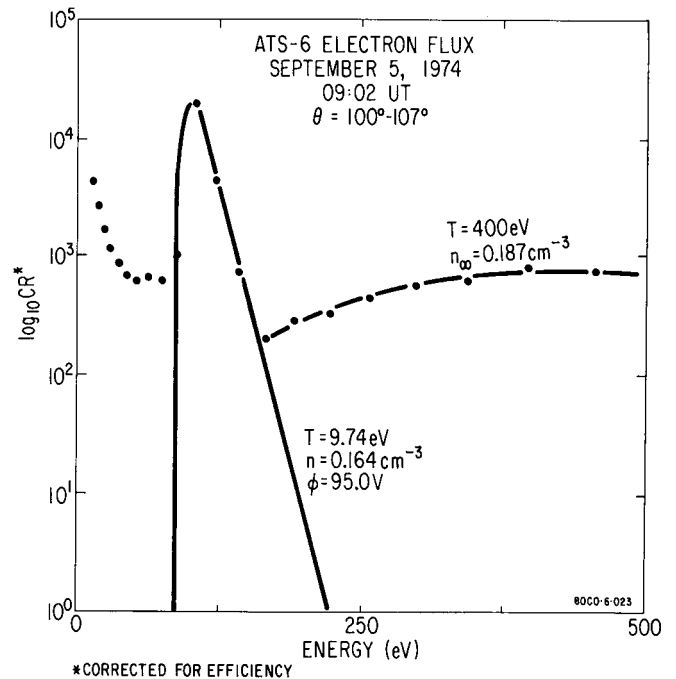


Fig. 14. Electron flux, September 5, 1974. The sharp spike and surrounding energy scan from the beginning of the previous figure is replotted here. The count rate has been corrected for various detector efficiency terms to facilitate modeling. An accelerated Maxwellian flux with parameters $T_e = 9.74$ eV, $n = 0.164$ cm⁻³, and $\phi = 95.0$ V is shown as the solid line through the peak, and a higher-energy Maxwellian is drawn through the ambient electron data, $T_e = 400$ eV, $n = 0.187$ cm⁻³.

low-energy electrons, then a large spike, followed by a broad bump of ambient electrons (about 20-keV temperature). The large spike is the 'differential charging spike' and is the flux of electrons seen in the spectrogram. The amplitude of the spike can be seen to vary with time, responding to the detector rotation.

The flux in this peak can be modeled as a Maxwellian distribution accelerated through a potential drop. Because the detector energy bins are large compared to the temperature of the distribution, it was useful to model the count rate (corrected for efficiency) rather than the distribution function. The results from such a model are shown in Figure 14. We see that the fluxes are well modeled by a 10-eV Maxwellian accelerated through a 95-V potential drop. The flux is equivalent to a -3 10-eV distribution with a density of 0.164 cm^{-3} . There is a good chance we are missing the center peak of the beam of electrons (in angle) and are underestimating the flux by a factor of 2-10. Also, the beam angular width is comparable to the detector aperture angular width (i.e., the measurement is not truly differential). Both these effects will tend to make our estimate of the flux a lower bound. The flux in the model Maxwellian is $8.6 \times 10^6/\text{cm}^2\text{s}$ at the source.

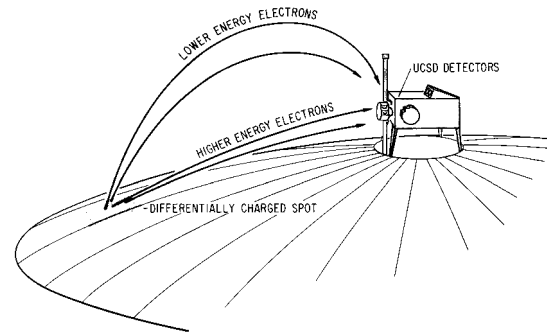


Fig. 16. Possible electron trajectories are shown from an early visualization of the problem of trapped electron fluxes. Higher-energy electrons take a straighter trajectory to the detector, and the detection angle should vary smoothly as the energy varies. Different sets of peaks in Figure 15 suggest different sources.

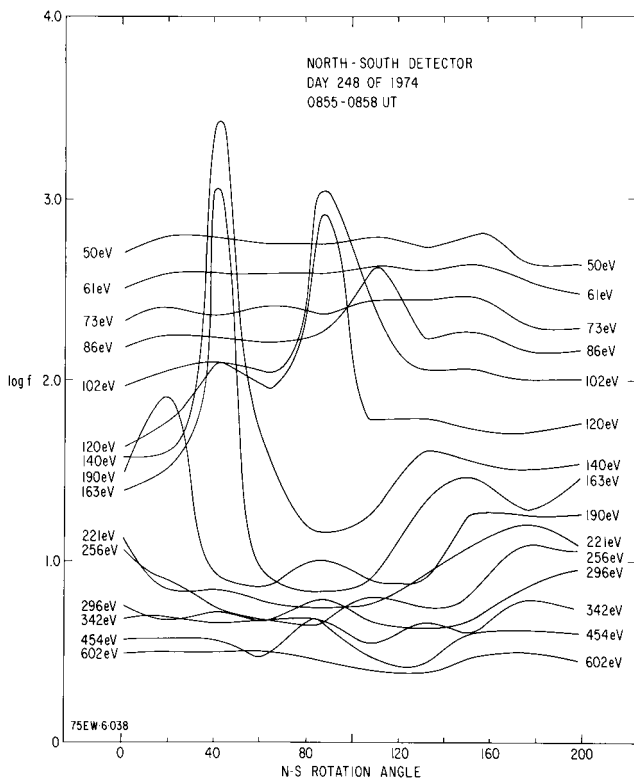


Fig. 15. Electron distribution functions, September 5, 1974. Electron distributions are plotted versus detector angle for energies between 50 eV and 600 eV. Data taken from 0855 to 0858 were similar to those shown in Figures 12-14.

The top of the spacecraft is in shadow at this time, and it is likely that these are secondary electrons and not photoelectrons. Secondary electron production is strongest for 100- to 1000-eV primary electrons. The ambient electron population in that energy range has a density of 0.2 cm^{-3} and a temperature of 400 eV, assuming a spacecraft potential of -191 V. If this distribution (decelerated by 286 V) is integrated over a secondary yield spectrum with a peak yield of 1 at 400 eV [Whipple, 1965], one obtains a secondary flux of $2.5 \times 10^7/\text{cm}^2\text{s}$. The peak at 400 eV is typical of many materials; the peak value of 1 is low by a factor of 2 compared to most materials. Thus the calculated secondary flux may also be somewhat low. Even so, it is within a factor of 3 of the observed flux.

Figure 15 shows 3 min of data reduced to distribution functions and plotted versus detector angle, with energy as a parameter. The largest peaks occur for 140-eV electrons at 40° detector angle and 102-eV electrons at 100° . The variation of the energy of the peak with detector angle can be explained in terms of the electron trajectories, as illustrated in Figure 16. Higher-energy electrons would take a more direct path to the detector and enter the detector at relatively low angles, while lower-energy particles enter at higher angles due to the relatively larger effect of the local electric fields. The presence of two distinct sets of curves with maxima in Figure 15 suggests the possibility of two distinct source areas at different potentials. Speculation about the source (or sources) of the spikes eventually centered upon the only insulating surfaces near the UCSD detectors, the University of Minnesota (UM) detectors. These small cubes were coated with an insulating white paint for thermal control. This speculation would have been limited to just that, but for the rotation of one of the two cubes. In the normal operating mode of these detectors, the detector furthest from ours rotated in 15° steps at 8-s intervals, covering a 180° range in 12 steps (13 positions).

On August 24 and 25 of 1974, the UCSD detector was in a unique mode, dwelling for long time periods at energies close to the barrier height.

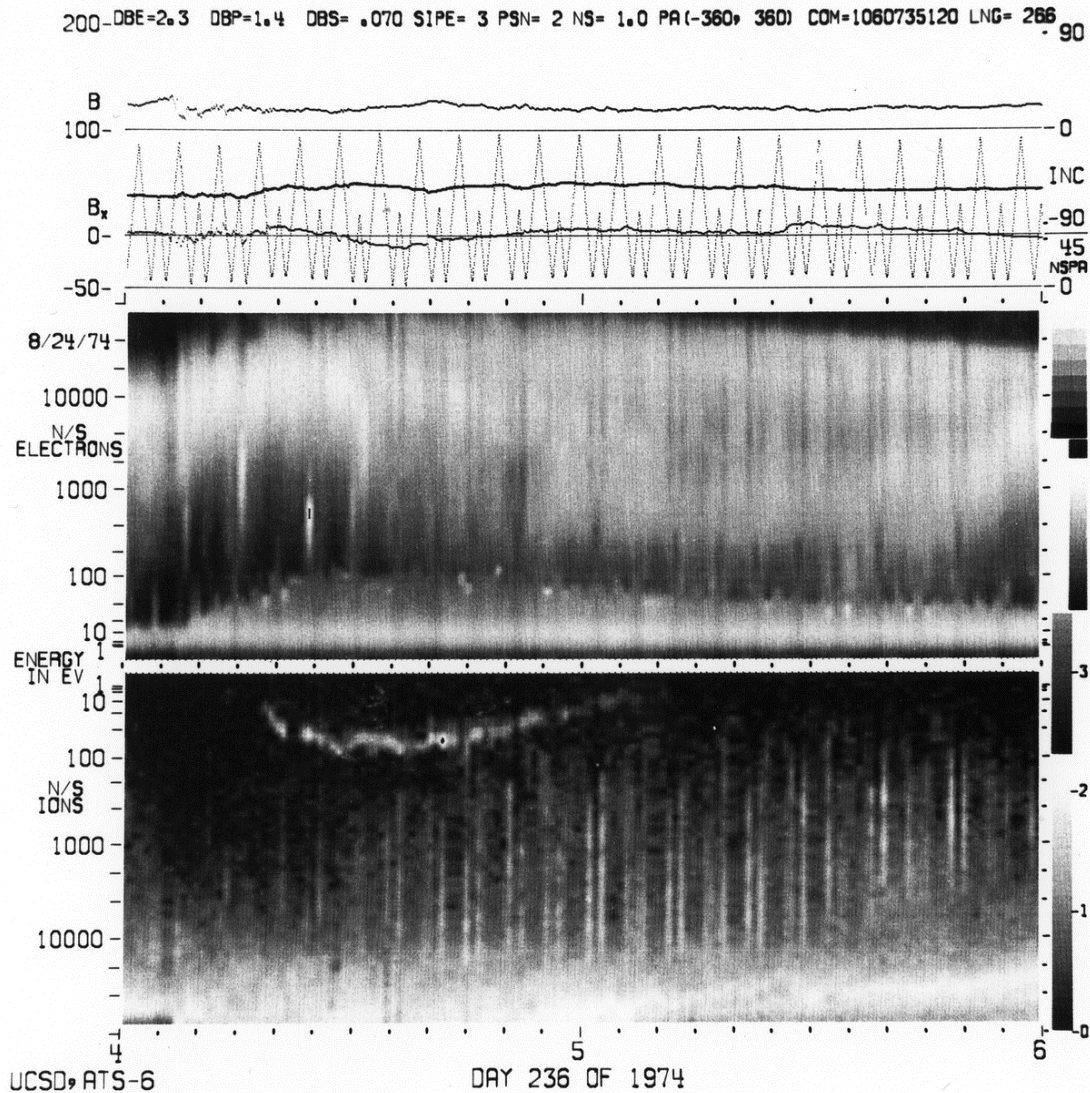


Fig. 17. Spectrogram for August 24, 1974, Two hours of data from the NS detector charging event. Potentials of -40 to -80 V are shown by ion data between 0420 and 0500 UT, accompanied by a differential charging barrier of about 100 V, as shown by the electrons.

Two hours of data from August 24 are shown in Figure 17. The spacecraft can be seen to charge negatively from 0420 to 0505, with differential charging also present during this time. Figure 18 shows the data taken at 61 eV when the UM detector rotated. The energy here is that of the charging spike, or accelerated electrons. The count rate increased by a factor of 5 in 50 ms, with a large spike that may represent the backlash in the UM rotational motion. Five other clear measurements were made over this 2-day period, which clearly correlated with the UM rotation. They show the same large transition, both up and down in flux. The gradual peaking of the data shows the effect of the UCSD detector rotation of 1.4° s. These changes in flux were not seen at all times on these 2 days. Some charging peaks showed no change when the UM detector rotated. This reinforces the idea of a separate source for some spikes, or at least a different face of the detector cube.

These data show that at least one of the sources observed by UCSD is a surface of the UM detector. There is a fair possibility that the stationary box is also a source of accelerated electrons. Having deduced large differential potentials on the dish antenna, it is not surprising that the UM detectors charge negatively when shadowed.

The detectors are apparently charging to a sufficient potential to allow normally emitted secondary electrons to escape the barrier region, permitting the insulated surfaces to achieve their own equilibrium with the plasma. Particles emitted with energies near the barrier height will follow distorted trajectories, as seen in Figure 9. Such particles can return to almost any point on the surface of the EME, or at a given point, with almost any angle. Statistical surveys of the data show that this is the case. Spikes are typically observed in the 100°-140° range, as in these data, but are seen at all angles in both detectors.

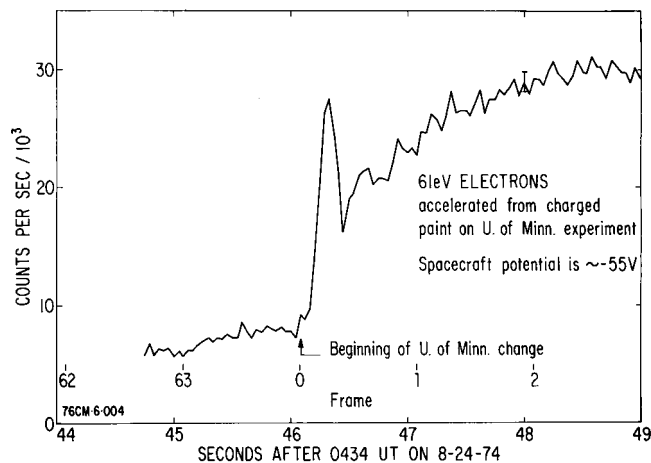


Fig. 18. Electron count rate plot for August 24, 1974. Data taken from the 61-eV channel of the NS electron detector are plotted versus time. The spacecraft potential is -55 V. Note that the count rate scale is linear and the time scale is in seconds. Timing of the UM rotation was obtained independently from spacecraft telemetry. The UCSD detector is rotating at 1.34° per second.

One final note is appropriate to this half of the study. At one time, it was thought that since the UM detector surface is clearly at a potential comparable to the barrier height, they might in some way be responsible for the barrier. This possibility was examined by means of the NASCAP potential solver. An accurate model of the EME package was constructed, with resolution such that the EME was 15 grid units in its largest dimension, and the UM boxes filled one grid box. It was found that because the UM detectors provide such a small percentage of the EME area, they simply could not provide a barrier over the EME. The UM detectors were concerned with particles of energies in excess of 20 keV, so they were not affected by the potentials the UCSD detectors reported on and around the UM cubes.

6. Summary

The observation of a barrier to charged particles has been explained as the result of differential charging on the spacecraft surface. The negative potentials deduced on shadowed insulators are smaller in magnitude than the potentials observed in eclipse but more negative than the observed mainframe potentials. The spherical and planar models are not particularly specific to the spacecraft and imply that such barriers will be seen on most spacecraft with shadowed insulators in these environments.

One source of accelerated electron fluxes was identified by changes in the flux caused by mechanical rotation. This phenomenon is again general and would be observed in most cases of charged insulators inside a barrier region.

The phenomena analyzed here suggest the strong need for electrostatic cleanliness in spacecraft at geosynchronous orbit. Reliable measurements of low-energy ambient plasma in the future will depend upon this condition.

Acknowledgments. The authors wish to thank Ray Walker for his help in establishing the behavior of the UM instrument and Bruce Johnson for his extensive analysis of the Minnesota Spots. This work was supported by contract NAS5-21055 and grant NSG-3150. The Editor thanks J. B. Reagan and A. G. Rubin for their assistance in evaluating this paper.

References

- Besse, A. L., and A. G. Rubin, A simple analysis of spacecraft charging involving blocked photoelectron currents, *J. Geophys. Res.*, 85, 2324-2328, 1980.
- Mandell, M. J., I. Katz, G. W. Schnuelle, P. G. Steen, and J. C. Roche, The decrease in effective photocurrents due to saddle points in electrostatic potentials near differentially charged spacecraft, *IEEE Trans. Nucl. Sci.*, 6(NS25), 1313, 1978.
- Mauk, B. H., and C. E. McIlwain, ATS 6 UCSD auroral particles experiment, *IEEE Trans. Aerosp. Electron. Syst.*, AES-11, 1125, 1975.
- Prokopenko, S. M. L., and J. G. Laframboise, Differential charging of geostationary spacecraft, *J. Geophys. Res.*, 85, 4125-4131, 1980.
- Whipple, E. C., Jr., The equilibrium electric potential of a body in the upper atmosphere and in interplanetary space, *NASA Tech. Note*, X-615-65-296, 1965.
- Whipple, E. C., Jr., Theory of the spherically symmetric photoelectron sheath: A thick sheath approximation and comparison with the ATS 6 observation of a potential barrier, *J. Geophys. Res.*, 81, 601, 1976a.
- Whipple, E. C., Jr., Observation of photoelectrons and secondary electrons reflected from a potential barrier in the vicinity of ATS 6, *J. Geophys. Res.*, 81, 715, 1976b.

(Received January 20, 1981;
revised March 23, 1981;
accepted March 23, 1981.)